ARTICLE

Open Access

Side-viewing axicon-integrated miniature fiber probe for extended depth of focus and ultrahigh lateral resolution endoscopic imaging

Yin Liu[1], Duanhong Zhang[2,3], Wenxin Li[2,3], Shicheng Zheng[4], Hong Fan[5], Tianyuan Lan[6,7], Qun Hao[2] and Yong Huang[2,3 ✉]

Abstract

The early and precise diagnosis of suspected pathological tissues or organs has increasingly embraced the utilization of 3D real-time visualization and discrimination of intricate structures facilitated by miniature optical coherence tomography (OCT) endoscopic probes. Those miniature side-viewing endoscopic fiber probes are indispensable for 3D imaging with small, narrow lumens, eliminating the potential for tissue trauma associated with direct-viewing techniques. Nevertheless, current manufacturing techniques pose limitations on the overall imaging prowess of these miniaturized side-viewing probes, hindering their widespread adoption. To surmount this challenge, an ultra-compact side-viewing OCT fiber-optic endoscopic probe with extended depth of focus (DOF) and high lateral resolution is designed based on the all-fiber composite structure. The quantitative relationship between the imaging performance and the fiber structural parameters has been theoretically analyzed. The imaging performance of the fiber probe can be flexibly tailored by adjusting the geometric parameters of the fiber-optic cascade structure. The applicability and feasibility of fiber probe prototype have been convincingly demonstrated through linear scanning and rotational scanning methodologies. This ultra-compact side-viewing OCT fiber probe's capacity to deliver microscopic structural insights paves the way for minimally invasive applications, expected to advance the frontier of early and precise diagnosis and treatment of suspected lesion tissues.

Keywords: quasi-Bessel Beam; high imaging performance; fiber-optic cascade structure; optical coherence tomography

Introduction

The primary impetus behind the advancement of OCT technologies stems from their unparalleled capability to conduct in situ imaging of tissue microstructures at histological resolution, obviating the necessity for tissue resection[1–3]. While OCT imaging has significantly contributed to minimally invasive diagnosis and treatment, challenges persist in imaging narrow lumens and organs, primarily due to limitations in visualization techniques[4,5]. This requires a practical and miniaturized high imaging performance solution that cannot only facilitate 3D scanning but also mitigate the risk of severe traumatic adverse events associated with endoscopic implantation. As a side-viewing OCT system with compact size and the ability to achieve circumferential scanning imaging features, it is a necessary condition for effectively achieving internal imaging of narrow lumen organs, rather than relying on dynamically curved fibers like direct-viewing probes to achieve 3D imaging[6,7]. The fiber-optic probe, when paired with OCT imaging technology, has garnered significant attention owing to its compact form factor, superior imaging quality, resistance to electromagnetic

Correspondence: Yong Huang (huangyong2015@bit.edu.cn)
[1]Beijing Engineering Research Center of Industrial Spectrum Imaging, School of Automation and Electrical Engineering, University of Science and Technology Beijing, Beijing, China
[2]Near-surface National Key Laboratory of Science and Technology on Near-surface Detection and Perception, Beijing Institute of Technology, Beijing, China
Full list of author information is available at the end of the article

interference, and robust biocompatibility. This combination holds immense potential for advancing medical imaging capabilities in challenging anatomical environments. It is worth noting that fiber probes combined with OCT imaging systems also have great potential in industrial and engineering fields[8,9], such as non-destructive testing of composite materials[10], monitoring of industrial surfaces and structures[11], surface/interface damage of industrial products or building structures[12], and defect detection of wafers and analysis of thin film microstructures[13].

When preparing fiber probe prototypes that necessitate extreme miniaturization, side-view imaging capabilities, and high imaging performance, manufacturing techniques face numerous constraints. Those constraints translate into intricate preparation procedures, compromised robustness, excessive sizes, and challenges in achieving both side-view imaging functionality and simultaneously meeting the requirements for high depth of focus (DOF) and low lateral resolution. This technical feature has become a daunting task. Connecting discrete optical devices with reflection and focusing functions to the fiber tip not only increases the overall dimension, but also poses additional challenges to installation and alignment[14–16]. Two-photon polymerization 3D printing technique based on femtosecond lasers is an alternative solution for manufacturing submicron-level components with complex shapes and low surface roughness[17,18]. However, the high cost and complex process steps of additive manufacturing equipment further hinder its application in large-scale manufacturing. The metalens based on artificial periodic nanostructure arrays has attracted widespread attention due to its ability to precisely control the optical phase[19–22]. Nevertheless, its integration onto fiber tips poses challenges, hindering further miniaturization of metalens-integrated fiber probes[22,23]. Having an appropriate preparation technique is a crucial prerequisite for the successful fabrication of the necessary side-viewing fiber probes, the demand for which is rapidly growing and becoming increasingly urgent.

In the design of traditional optical focusing devices, high lateral resolution imaging guaranteed by a large numerical aperture will lead to rapid dispersion of illumination focused beams, resulting in smaller DOF[24–27]. A good design attempts to find the best compromise between sufficient DOF and lateral resolution[28–33]. Axicon at the fiber tip can transform Gaussian beams transmitted into Bessel–Gaussian beams. This quasi-Bessel beam has non-diffraction characteristics and can maintain a small focused spot over long propagation distances, achieving both large DOF and high lateral resolution in endo-OCT system[34–38]. However, the fiber-optic axicon-integrated device is mainly used in direct-viewing probes[39–41]. The full potential of this optical device in the field of endoscopic side-view imaging has not been fully utilized.

To address the pressing need for side-viewing fiber probes with compact, large DOF, and high lateral resolution, we demonstrated a fiber-optic OCT imaging probe based on a sizable axicon and spot reflector embedded within fiber microsphere. The fiber probe prototype has advantages such as large focusing depth (~349.8 μm), high lateral resolution (~1.4 μm), and compactness (~591 μm in outer diameter, ~1707 μm in effective length). Its performance and conversion potential are demonstrated by imaging in vitro animal tissues. The proposed fiber probe has paved the way for the expansion of side-viewing fiber-optic endoscopes to the study of disease mechanisms in biomedical science and clinical research.

Results

Design of fiber microprobe with side-view imaging function

The design diagram of the fiber probe for side-view imaging is shown in Fig. 1a. The miniature side-viewing fiber probe consists of single-mode fiber (SMF), large-diameter no core fiber (LDNCF), fiber microsphere, reflector, and fiber axicon. The LDNCF, as an illumination beam expander, serves as a connector between SMF and fiber microsphere. UV-curing adhesive is used to solidify the fiber microsphere and LDNCF. The reflector embedded in a fiber microsphere can achieve the conversion of the illumination beam and the scattered collection beam between axial and radial directions of the fiber probe. The axicon located on the fiber microsphere coincides with the spot of the illumination beam reflected by the reflector. The function of the fiber microsphere is not only to provide a substrate for the reflector and axicon, but also to further expand the illumination beam.

Simulation of fiber probe illumination beam

To facilitate the calculation of the focusing characteristics of the illumination beam and reduce the computational burden, the optical design of the fiber probe has been simplified (see "Methods" section). The side-viewing fiber probe has been simplified into an equivalent direct-view imaging fiber probe (Fig. 1b inset) with the basic structure being the SMF-LDNCF-microsphere-axicon cascaded structure. Considering the beam transmission characteristics of the fiber microsphere and the material consistency, the fiber microsphere is simplified into a large-diameter cylindrical waveguide in the simplified fiber probe model, and the reflector and the UV-curing adhesive layer are ignored. The finite difference beam propagation method (FD-BPM) was used to simulate the transmission of an illumination beam with a central wavelength of 1310 nm in a simplified forward-viewing fiber probe and the focusing characteristics of the illumination beam outside the fiber probe, as shown in Fig. 1b. Figure 1b inset illustrates the light field intensity
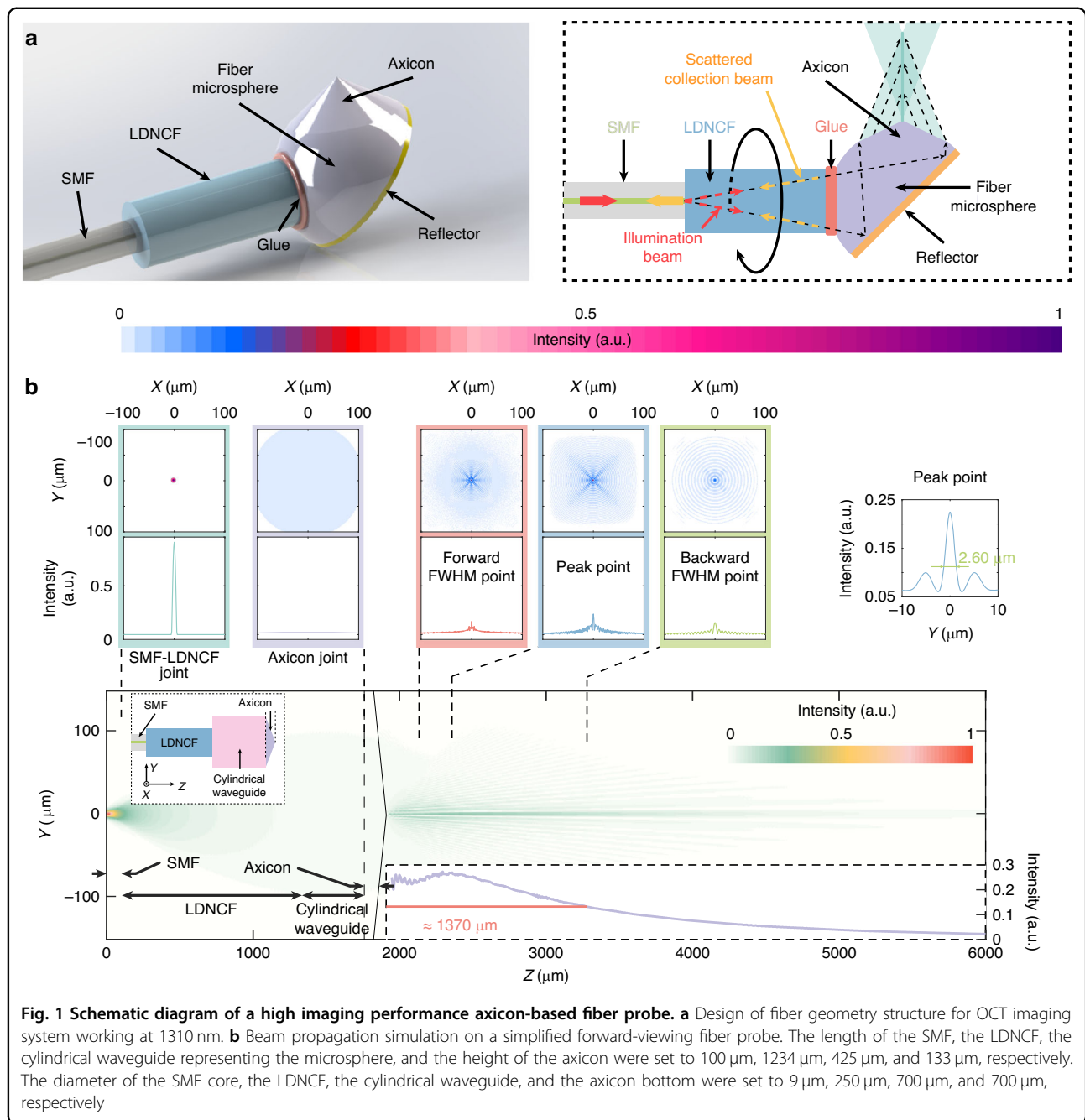
Fig. 1 Schematic diagram of a high imaging performance axicon-based fiber probe. a Design of fiber geometry structure for OCT imaging system working at 1310 nm. **b** Beam propagation simulation on a simplified forward-viewing fiber probe. The length of the SMF, the LDNCF, the cylindrical waveguide representing the microsphere, and the height of the axicon were set to 100 μm, 1234 μm, 425 μm, and 133 μm, respectively. The diameter of the SMF core, the LDNCF, the cylindrical waveguide, and the axicon bottom were set to 9 μm, 250 μm, 700 μm, and 700 μm, respectively

distributions at the SMF-LDNCF connection point, the incident axicon, and the front forward width half maximum (FWHM), peak, and backward FWHM points of the illumination beam. The FWHM range of the axial focused beam, i.e., the DOF of the OCT imaging system, is ~1370 μm, and the diameter of the focused spot@FWHM, i.e., the lateral resolution of the OCT imaging system, is ~2.6 μm.

The simulation (Fig. 1b) using FD-BPM is carried out under the assumption of the illumination beam being coaxial with the fiber axicon. However, in reality, the mismatch between the fiber axicon and the illumination beam spot will cause the generated quasi-Bessel beam to deviate from the cone axis. Those deviations in the actual size, angle, and alignment, compared to the intended design specifications, arise due to processing and installation inaccuracies in elements such as LDNCF, fiber microsphere, axicon, and reflective surface. These inaccuracies lead to a misalignment between the axicon and the illumination beam spot, ultimately causing the generated quasi-Bessel beam to stray from the predetermined conical axis. The *YZ*-plane and *XY*-plane intensity
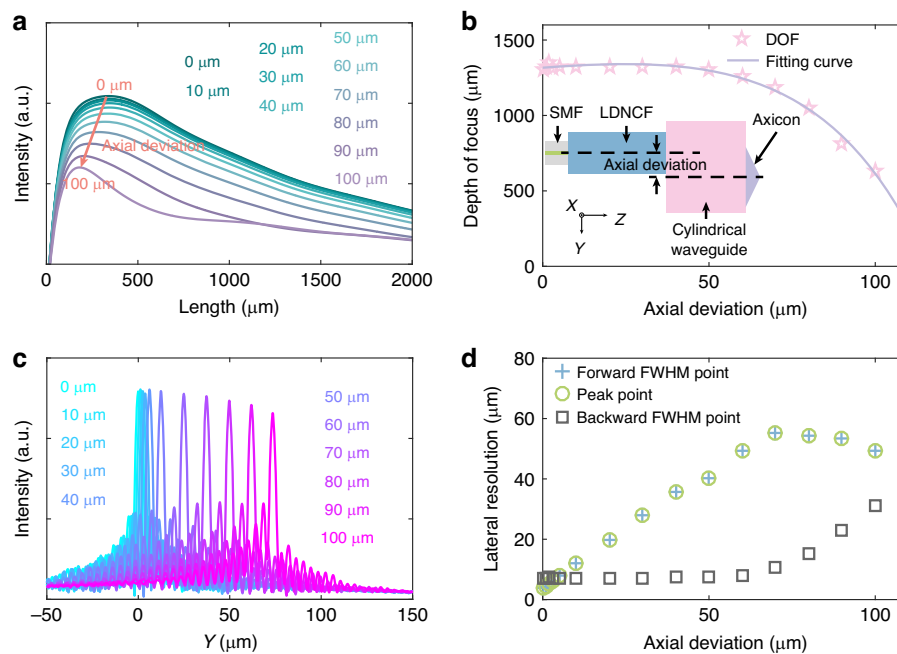
Fig. 2 FD-BPM simulation results in the imaging performance of a simplified direct-viewing probe. a Variation of optical field intensity in the main lobe propagation direction under different axial deviations. **b** Evolution relationship between axial deviation and DOF. **c** Beam profiles at the peak intensity of the main lobe with different axial deviations. **d** Lateral resolution at the peak and FWHM intensity points
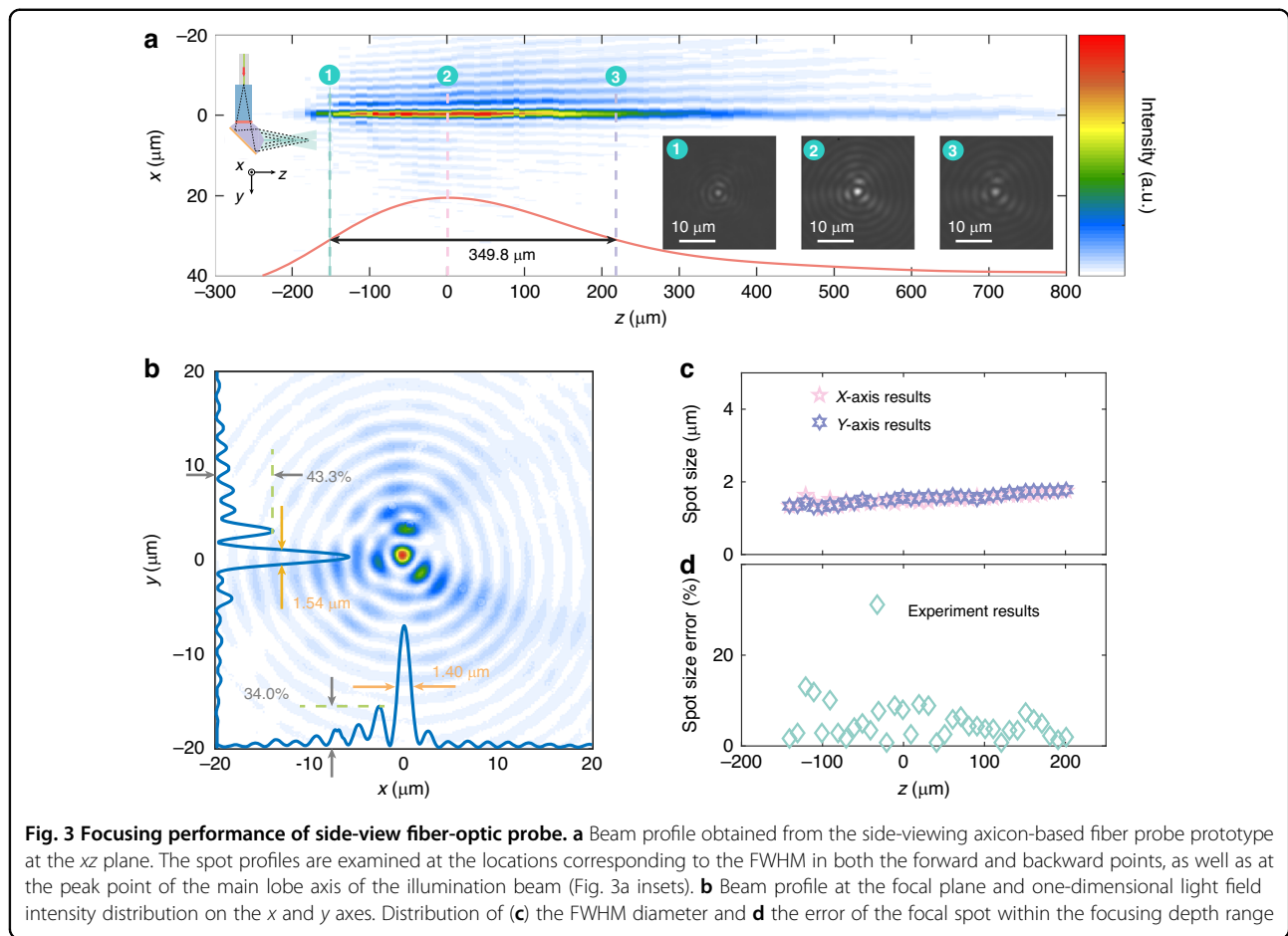
distributions were shown in Figs. S1 and S2 of the Supplementary Materials at different axial deviations, respectively. It can be seen from Figs. S1 and S2 that as the axial deviation increases, the distribution of the axicon *YZ*-plane and *XY*-plane will undergo drastic changes.

The intensity of the main lobe of the quasi-Bessel beam under different axial deviations is shown in Fig. 2a, and as the axial deviation increases, the overall intensity decreases. This may be because, as the non-overlapping areas increase, the variation in the incidence angle of the illumination beam will lead to additional optical path difference, a decrease in the amount of light that meets the phase matching conditions, and thus a decrease in overall strength. As the axial deviation increases, indicating a decrease in the DOF of the fiber probe (Fig. 2b). This may be due to a decrease in the effective incident area of the axicon, accompanied by an increase in axial deviation. At varying degrees of axial deviation, the one-dimensional intensity profile corresponding to the peak spot location is depicted in Fig. 2c. The variation in the distance between the main lobe and the cone axis follows a consistent trend with the change in axial deviation. This may be due to the increase in non-interfering light as the axial mismatch increases. The relationship between the axial deviation and the lateral resolution at the forward and backward FWHM positions and peak points of the main lobe axis is shown in Fig. 2d. As the axial deviation increases, the FWHM diameter of the forward and

backward points first rises and then slightly falls, while that of the backward point slowly rises first and then rapidly rises. The reason for the above phenomenon may be due to the combined effect of the oblique incidence of the illumination beam and the variation of the effective working area with axial deviation. It can be clearly seen from Fig. 2d that in the case of a small mismatch, a relatively consistent focusing spot FWHM diameter (lateral resolution) can be maintained within the focusing imaging range.

Focusing characteristics of fiber probe prototype

The preparation method of the fiber probe can be found in the "Methods" section. To demonstrate that the side-viewing fiber probe can achieve high lateral resolution within a large focusing depth range, experimental characterization and analysis were conducted. The 3D optical field intensity distribution of the output illumination beam can be obtained by stacking the *xy*-plane spots at different positions in spatial order along the *z* axis (see Supplementary Materials section III). The imaging performance is assessed through the evaluation of the main lobe FWHM distance, referred to as the DOF, as well as the *xy*-plane spot FWHM diameter, indicative of the lateral resolution. The point of the main lobe peak intensity is set to the *z* axis origin. Figure 3a shows the profile of the illumination beam in the *xz*-plane, with a DOF of 349.8 μm for the quasi-Bessel beam main lobe. Compared
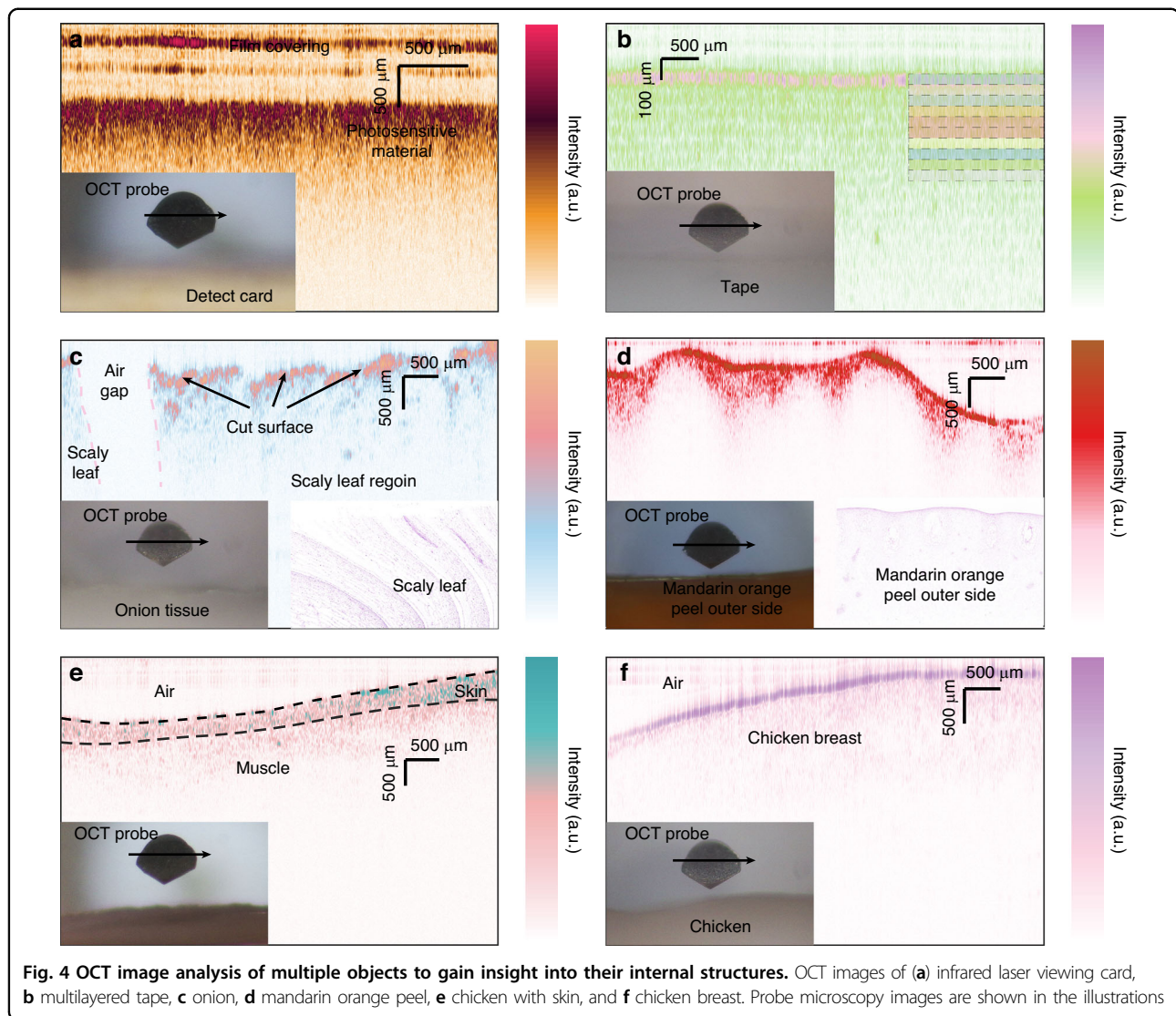
Fig. 3 Focusing performance of side-view fiber-optic probe. a Beam profile obtained from the side-viewing axicon-based fiber probe prototype at the *xz* plane. The spot profiles are examined at the locations corresponding to the FWHM in both the forward and backward points, as well as at the peak point of the main lobe axis of the illumination beam (Fig. 3a insets). **b** Beam profile at the focal plane and one-dimensional light field intensity distribution on the *x* and *y* axes. Distribution of (**c**) the FWHM diameter and **d** the error of the focal spot within the focusing depth range

with the typical direct-viewing SMF conical probe with a DOF of about 30 μm[35], the DOF is increased by about 11 times.

The focal spot measured on the *xy*-plane at the peak position of *z* axis strength is shown in Fig. 3b. The focal spot has an almost symmetrical contour; the estimated FWHM diameter of *x* axis and *y* axis are ~1.40 μm and 1.54 μm, respectively. The astigmatism ratio (the ratio of the *x* axis/*y* axis FWHM diameter) is about 0.9, signifying an acceptable level. The sidelobe intensity in the *x* axis and *y* axis directions is ~34.0% and 43.3% of the main lobe intensity, respectively. The focused-plane illumination beam profile in Fig. 3b clearly exhibits the characteristic features of a Bessel beam alongside imperfect sidelobes. These imperfections may arise from manufacturing errors in the axicon and misalignment in the fiber components. In terms of axicon fabrication, apex angle deviations and surface roughness introduce wavefront distortions, resulting in asymmetric sidelobe intensity distributions. Misalignment between the propagation direction of the illumination beam and the optical axis of the axicon induces higher-order modes, exacerbating sidelobe interference. Further minimizing manufacturing errors in

axicons and optimizing component alignment can mitigate these imperfections. To reduce the sidelobe intensity of the Bessel beam, a multi-stage axicon structure can be employed. By segmenting and optimizing phase distributions across different regions, such structures suppress sidelobe generation. An excessively large apex angle in the fiber axicon causes an abrupt phase change at the edge, potentially intensifying sidelobes. Reducing the apex angle or adopting a graded apex angle design can balance energy distribution between the main lobe and sidelobes. Enhancing surface fabrication precision in fiber axicons minimizes phase errors caused by surface defects, thereby lowering sidelobe intensity. Additionally, aligning the divergence angle of the incident beam with the axicon design parameters helps avoid phase mismatches due to excessive divergence, thereby further reducing sidelobe interference.

Figure 3c shows the distribution of the FWHM diameter of the focused spot in the *z* axis direction within the FWHM intensity range of the main lobe. The lateral resolution remains below 1.8 μm within the DOF range of ~350 μm. These results prove that achieving high lateral resolution under extended focusing depth is feasible. The

Fig. 4 OCT image analysis of multiple objects to gain insight into their internal structures. OCT images of (**a**) infrared laser viewing card, **b** multilayered tape, **c** onion, **d** mandarin orange peel, **e** chicken with skin, and **f** chicken breast. Probe microscopy images are shown in the illustrations

FWHM diameter deviation of the focused spot, both in the x- and y directions, is <15%, as depicted in Fig. 3d. This aspect can be further refined through the ongoing enhancement of the fiber probe process steps and manufacturing equipment. From the comparison of performance parameters between the proposed side-viewing fiber probe and direct-viewing fiber probes (Table S1, in the Supplementary Materials), the proposed probe avoids chemical damage through hot melting and grinding, and has excellent imaging performance.

Microprobe linear scanning imaging

To comprehensively assess the applicability and practicality of combining the proposed fiber probe with a spectral domain OCT (SD-OCT) imaging system (see "Methods" section), it is imperative to employ a diverse array of test samples. Utilize an electric linear displacement platform to translate the fiber probe in the X-direction, subsequently

capturing two-dimensional cross-sectional images (B-scans) on test samples. Figure 4a depicts the internal structure of the infrared laser detector card, which has a thin film cover and an organic layer. OCT images can clearly distinguish the internal structure. The thickness of the semi-transparent tape is ~50 μm. From Fig. 4b, we can clearly observe that over 10 layers of tape, the imaging depth in stacked tape samples may exceed 500 μm. The tissue cross-sections of onion (Fig. 4c), orange peel (Fig. 4d), chicken skin (Fig. 4e), and chicken breast (Fig. 4f) were imaged. The slight blurring of the OCT imaging structure may be caused by damage to the internal structure during the cutting process. From Figs. 4c–f, the internal structure of these organizations can be easily identified.

Microprobe rotational scanning imaging

The intramuscular fat (IMF) intensity of absorbing infrared light is about 9 times that of muscle, facilitating

an accurate estimation of fat content in meat samples[42]. The side-viewing fiber-optic probe prototype can change the traditional meat quality assessment, achieving non-contact and non-destructive classification. The relationship between the total backscattered light reflected by the meat sample and the depth of the scatterer and the attenuation coefficient can be obtained through the Beer-Lambert law[43]. The attenuation coefficient describes the exponential decay of illumination light incident on the meat sample, which can be easily obtained from the A-scan as a depth function and used to distinguish IMF from muscle. It is worth noting that it only relies on qualitative differences rather than absolute values. B-scan images of different meat samples are used to elucidate this aspect in Fig. 5a–d. Samples of chicken (breast), beef (tenderloin), pork (hind legs), and mutton (tenderloin) were selected for side-viewing rotation OCT image acquisition. The optical microscopy images during probe rotation imaging and the haematoxylin and eosin (H&E) staining images of different meat samples are shown in their respective illustrations. Selecting an A-scan of different raw meat samples at the center position (Fig. 5e). The gradient of the feature best-fit line enables the estimation of the attenuation coefficients of muscle and IMF. The absorption of 1310 nm wavelength illumination light by IMF is more pronounced compared to that of muscle tissue or water. This difference can be detected in the OCT signal for tissue identification with different IMF content. To reduce the complexity and dimensionality, a small area (100 pixels * 100 pixels) within the same distance from the fiber probe is selected, and the OCT signal strength in the area is converted into an intensity quantity histogram. The histograms within the same distance and pixel count area for different meats are shown in Fig. 5f. Those meat samples with low effective attenuation coefficients have a smoother voxel distribution, i.e., more dispersed. Therefore, meat samples with high IMF content are expected to have more voxels on the high side of the effective attenuation coefficient histogram. OCT imaging holds significant potential for meat classification and quality assessment. By integrating the fiber probe with OCT technology, meat samples can be scanned non-destructively to acquire high-resolution 2D or 3D feature images. Concurrently, label information, such as meat type, cut, and quality grade (e.g., IMF content and tenderness score), is recorded to construct a labeled dataset. The collected OCT images undergo preprocessing and enhancement to optimize data quality. Subsequently, a model combining classification and regression is developed to identify meat types and evaluate quality, employing either traditional machine learning or deep learning approaches. This framework ultimately offers the meat industry an efficient, non-destructive solution for classification and quality assessment.
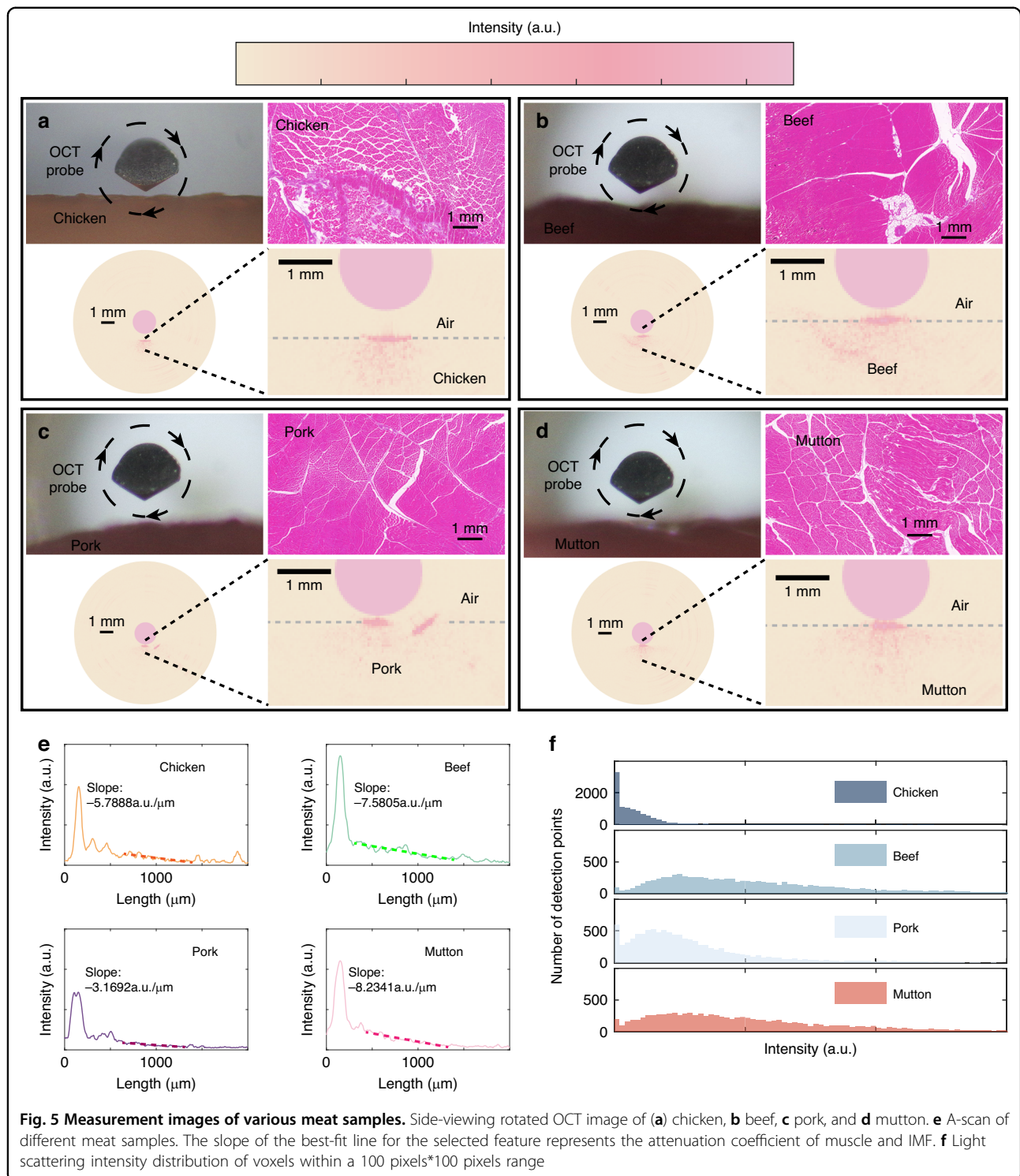
To evaluate the performance of this side-view imaging fiber probe in 3D scanning narrow lumen tissue samples, images of the thawed trachea and esophagus of chickens and quails in vitro, purchased from supermarkets, were analyzed. In order to protect the fiber probe during rotation and retraction, a transparent protective sleeve is wrapped around the fiber probe (Fig. 6 inset). Although the trachea and esophagus show severe stenosis, the fiber probe effortlessly passes through the esophagus and trachea and smoothly rotates and retracts. From Fig. 6a–d, it can be seen that OCT images demonstrate the characteristics of these tissues. The blurring of the OCT image may be caused by protein denaturation of the trachea and esophagus due to freezing.

Discussion

In this study, a compact fiber-optic endoscopic probe has been devised that can achieve side-viewing OCT imaging. This fiber probe accomplishes the transformation of the illumination beam and scattering acquisition beam from axial to radial, and vice versa, through the utilization of a reflector integrated within the fiber microsphere. Notably, the sizable axicon featured on the microsphere converts the illumination beam into a quasi-Bessel beam, which boasts non-diffraction and self-healing properties. This enables the illumination beam to maintain a narrow focus spot FWHM diameter over an extended propagation distance. When integrated with an OCT imaging system, this probe exhibits exceptional DOF and high lateral resolution.
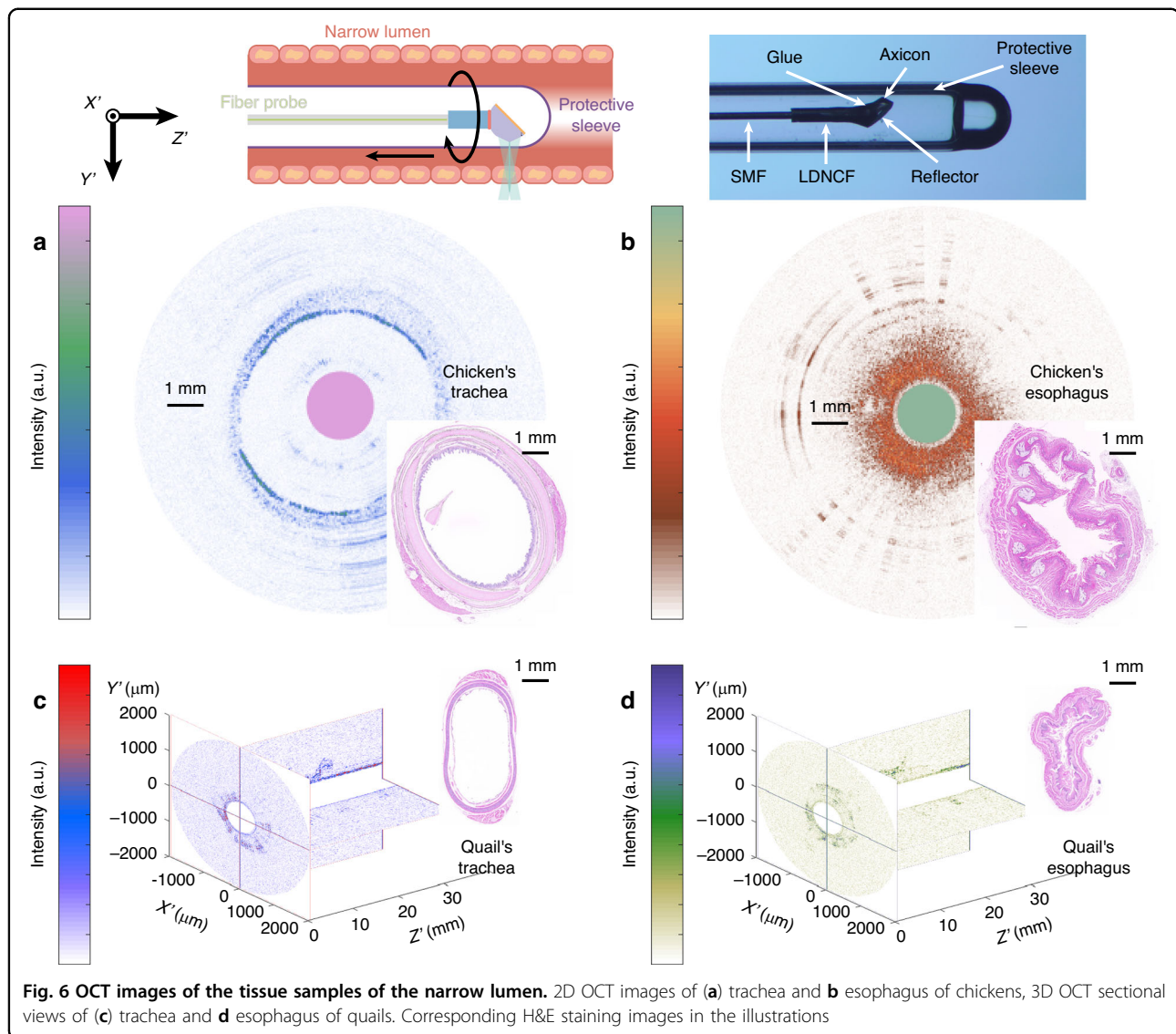
In principle, the multilayered structure present in the optical path from the SMF core tip to the focused spot will reduce the focusing quality[23]. For example, the use of protective sheaths at the remote end tends to result in more severe distortion of the focused spot. The protective sleeves, due to their differing curvatures parallel and perpendicular to the fiber probe axis, introduce astigmatism[36]. Given the challenges in adjusting the shape and refractive index (RI) distribution of the focusing element, these significant limitations cannot be corrected in current OCT catheter designs. Furthermore, the technical difficulties associated with transmitting the illumination beam inside the fiber probe itself complicate the process of addressing the aforementioned limitations even more. Grinding the cone into an asymmetric elliptical shape might offer a more viable solution[44].

Metasurface/metalens and 3D nano-printing technologies offer transformative potential for fabricating complex fiber tips, addressing the limitations of conventional fiber processing methods in flexibility, controllability, and scalability. Metasurface/metalens exhibit unparalleled advantages in precise phase modulation of light beams, making them particularly suitable for applications requiring tailored optical properties, such as wavefront

Fig. 5 Measurement images of various meat samples. Side-viewing rotated OCT image of (**a**) chicken, **b** beef, **c** pork, and **d** mutton. **e** A-scan of different meat samples. The slope of the best-fit line for the selected feature represents the attenuation coefficient of muscle and IMF. **f** Light scattering intensity distribution of voxels within a 100 pixels*100 pixels range

shaping and polarization modulation. The commercialization services of 3D nano-printing have further lowered the barrier to implementation. However, achieving large-scale industrial production necessitates either enhanced technological maturity or alternative solutions, as current trade-offs between cost, precision, and throughput remain unresolved. For example, fiber grinding techniques remain economically viable for standardized probe mass production, whereas 3D nano-printing and metasurface/metalens excel in high-precision, customized scenarios. Future advancements may lie in hybrid methodologies that synergize fiber processing with metasurface

Fig. 6 OCT images of the tissue samples of the narrow lumen. 2D OCT images of (**a**) trachea and **b** esophagus of chickens, 3D OCT sectional views of (**c**) trachea and **d** esophagus of quails. Corresponding H&E staining images in the illustrations

engineering and 3D printing. Such integration could balance flexibility and cost-effectiveness while leveraging the complementary strengths of each technology.

It is noteworthy that the fabrication process of the side-viewing fiber probe prototype relies solely on standard and widely available fiber processing techniques. This streamlined process ensures scalability, allowing for potential mass production. The fiber probe showcases a compact design with an impressively small functional tip volume of ~0.468 mm^3. In cost considerations, the prices of SMF, LDNCF, and NCF are approximately $30.0/km, $3.5/m, and $2.1/m, respectively. The total cost of fibers and consumables utilized in constructing the entire fiber probe remains well below $1. Regarding production equipment, a fiber-optic fusion splicer, a fiber microsphere burning system, a precision fiber cutting system, a fiber grinding and polishing system, and an alignment coupling system form the complete self-constructed production arsenal. The cumulative cost of this equipment does not exceed ~$8000, making the entire production process both efficient and economical. Consequently, the designed fiber probe boasts not only low-cost production but also the capability for large-scale manufacturing, simplicity in production processes, and significant commercial potential. The proposed side-view fiber probe has made significant contributions to the field through three key advancements: fiber probe design methodologies, a theoretical framework for validating structure-performance relationships, and standardized fabrication protocols that bridge the gap between miniaturization demands and practical implementation. While absolute performance optimization remains an area for future research, the probe's cost-effectiveness, scalability, and adaptability underscore its unique value proposition
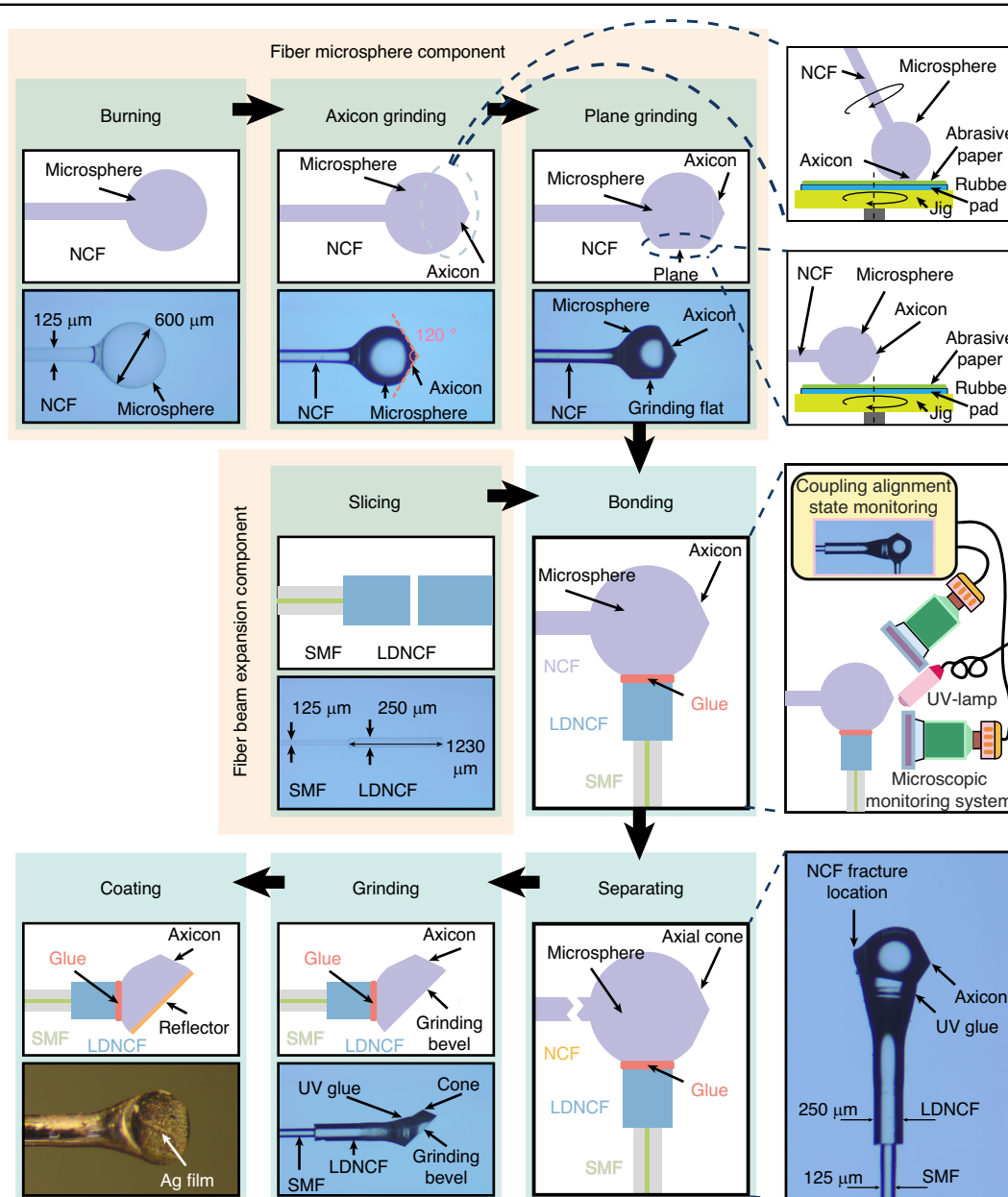
Fig. 7 Preparation process of side-viewing axicon-based fiber-optic OCT probe

in emerging applications where conventional solutions are inadequate.

In summary, a fiber OCT probe prototype that boasts side-view imaging capabilities, coupled with an exceptional combination of a large DOF and high lateral resolution, has been developed. The imaging prowess of this fiber probe has undergone systematic characterization and experimental validation. Furthermore, we have showcased its versatility through linear and circumferential scanning imaging. To emphasize the probe's adaptability for imaging within narrow lumens and its potential for diverse applications, the fiber probe with a diameter of less than 1.1 mm, post-protective

packaging was employed. This enabled the achievement of 2D/3D imaging within the trachea and esophagus of chicken/ quail. This cost-effective yet high-performance fiber probe introduces an impactful tool for 3D OCT imaging, presenting a promising avenue for biopsy studies involving narrow lumens in pediatric or young patients.

Methods
Implementation and design considerations for OCT endoscopic probe

The optical design of the side-viewing axicon-based fiber probe can be simplified to an equivalent direct-

viewing fiber probe (Fig. S3 of the Supplementary Materials). The DOF of the equivalent direct-viewing fiber probe can be expressed as refs. [29,45]:

$$DOF = \omega_0[\cot(\delta) - \cot(\tfrac{\theta}{2})]$$

$$= \frac{\tan\frac{\theta}{2} \tan\left(\arcsin\frac{NA}{n_{\mathrm{NCF}}}\right)\left(R_{\mathrm{Ball}}+L_{\mathrm{NCF}}+L_g+l_{\mathrm{Ball}}\right)}{\tan\frac{\theta}{2}+\tan\left(\arcsin\frac{NA}{n_{\mathrm{NCF}}}\right)}$$

$$\left[- \tan\left(\frac{\theta}{2} + \arcsin\left(\frac{n_{\mathrm{Ball}}}{n_{\mathrm{env}}} \cos\left(\frac{\theta}{2} + \arcsin\frac{NA}{n_{\mathrm{NCF}}}\right)\right)\right) - \cot\frac{\theta}{2}\right] \tag{1}$$

where L_{NCF}, L_g, l_{Ball}, and R_{Ball} are the length of LDNCF, the thickness of UV adhesive layer, the distance from the center of the fiber microsphere to the UV adhesive layer, and the fiber microsphere radius, respectively. NA, δ, and θ are the numerical aperture of SMF, the angle between the cone axis and the refracted beam at the axicon-environment interface, and the fiber axicon angle, respectively. n_{NCF}, n_{Ball}, and n_{env} are the RI of LDNCF, fiber microsphere, and environment, respectively. The lateral resolution of the equivalent direct-viewing fiber probe can be expressed as:

$$R_{\mathrm{S}} = \frac{2.048\lambda}{2\pi \sin(\delta)}$$

$$= \frac{2.048\lambda}{-2\pi \cos\left(\frac{\theta}{2}+\arcsin\left(\frac{n_{\mathrm{Ball}}}{n_{\mathrm{env}}} \cos\left(\frac{\theta}{2}+\arcsin\frac{NA}{n_{\mathrm{NCF}}}\right)\right)\right)} \tag{2}$$

However, the reflector angle also plays a crucial role in the imaging performance of the fiber probe. In order to address the deficiencies inherent in the equivalent direct-viewing probe model and to gain a profound comprehension of how the structural parameters of the side-viewing fiber probe influence its imaging capabilities, we have derived the imaging performances of this fiber probe (Fig. S4 of the Supplementary Materials). The interdependence of the DOF, lateral resolution, and the fiber geometric structure parameters of the axicon-integrated side-viewing fiber probe is elucidated in Eqs. (E1–E6) of the Supplementary Materials.

Manufacturing process of the fiber probe

The prototype development of a fiber probe necessitates the fabrication of two key components: a functional fiber microsphere component and a fiber beam expansion component. By seamlessly integrating these two components, the fiber probe acquires the capability of performing side-view imaging (Fig. 7). The step-by-step procedure for constructing the fiber probe prototype is thoroughly outlined in Section V of the Supplementary Materials. In the side-viewing fiber probe prototype, the length of LDNCF, the fiber microsphere radius, the distance between the bonding plane and the center of the microsphere, the angle between the reflection angle, and

the fiber axicon angle were set to 1230 μm, 300 μm, 200 μm, 45°, 120°, respectively.

1310 nm SD-OCT endoscopy system

SD-OCT system is used to demonstrate the performance of the side-viewing axicon-based probe. A detailed description of the SD-OCT system can be found in the Supplementary Materials Section VI. To achieve the side-view 3D imaging function, a self-made rotating module based on a servo motor driving the rotation of the fiber-optic slip ring is used to perform the fiber probe for 360° circumferential scanning imaging. Spiral motion can be accurately transmitted from the distal end, composed of a servo motor, fiber-optic slip ring, and linear electric displacement platform, to the proximal end, thereby achieving 3D scanning of the fiber probe.

Author details
[1]Beijing Engineering Research Center of Industrial Spectrum Imaging, School of Automation and Electrical Engineering, University of Science and Technology Beijing, Beijing, China. [2]Near-surface National Key Laboratory of Science and Technology on Near-surface Detection and Perception, Beijing Institute of Technology, Beijing, China. [3]Yangtze Delta Region Academy of Beijing Institute of Technology, Jiaxing, Jiaxing, Zhejiang, China. [4]Department of Gastroenterology, West China Longquan Hospital Sichuan University & The First People's Hospital of Longquan Yi District, Chengdu, Sichuan, China. [5]Shenzhen Urban Public Safety and Technology Institute, Shenzhen, Guangdong, China. [6]China General Nuclear Power Design Co., Ltd.(Shenzhen), Shenzhen, China. [7]State Key Laboratory of Nuclear Power Safety Monitoring Technology and Equipment, Shenzhen, China

Data availability
Data underlying the results presented in this paper are not publicly available at this time but may be obtained from the authors upon reasonable request.

Competing interests
The authors declare no competing interests.

References
1. Qi, J. et al. National and subnational trends in cancer burden in China, 2005–20: an analysis of national mortality surveillance data. *Lancet Public Health* **8**, e943–e955 (2023).
2. Jassim, A. et al. Cancers make their own luck: theories of cancer origins. *Nat. Rev. Cancer* **23**, 710–724 (2023).

3. Zhou, M. et al. Mortality, morbidity, and risk factors in China and its provinces, 1990-2017: a systematic analysis for the Global Burden of Disease Study 2017. *Lancet* **394**, 1145–1158 (2019).

4. Araki, M. et al. Optical coherence tomography in coronary atherosclerosis assessment and intervention. *Nat. Rev. Cardiol.* **19**, 684–703 (2022).

5. Badt, N. & Katz, O. Real-time holographic lensless micro-endoscopy through flexible fibers via fiber bundle distal holography. *Nat. Commun.* **13**, 6055 (2022).

6. Pleskow, D. K. et al. In vivo detection of bile duct pre-cancer with endoscopic light scattering spectroscopy. *Nat. Commun.* **14**, 109 (2023).

7. Choi, W. et al. Flexible-type ultrathin holographic endoscope for microscopic imaging of unstained biological tissues. *Nat. Commun.* **13**, 4469 (2022).

8. Sun, T. et al. In-situ monitoring of hole evolution process in ultrafast laser drilling using optical coherence tomography. *J. Manuf. Process.* **133**, 1290–1299 (2025).

9. Liu, Y. et al. Test-time image reconstruction for cross-device OCT fingerprint extraction. *IEEE Trans. Inf. Forensics Secur.* **20**, 1049–1064 (2024).

10. Ni, Z. et al. Measuring polymerization shrinkage of dental composite by using PhS-OCT. *Measurement* **221**, 113471 (2023).

11. Chays, F. et al. Development of an OCT system for measuring machining defects on a texturing laser machine. *Procedia CIRP* **113**, 570–575 (2022).

12. Minami, M. et al. In-situ investigation on crack-initiation and deformation of Al2O3 green bodies during dewaxing process by combined OCT-TG-FTIR and TMA. *Ceram. Int.* **49**, 15387–15394 (2023).

13. Shi, F. et al. Polarized laser scattering detection of low-density and micronscale subsurface cracks in silicon wafer. *Precis. Eng.* **86**, 75–81 (2024).

14. He, B. et al. Robotic-OCT guided inspection and microsurgery of monolithic storage devices. *Nat. Commun.* **14**, 5701 (2023).

15. Wang, J. et al. A generic and effective system dispersion compensation method: development and validation in visible-light OCT. *Photonics* **10**, 892 (2023).

16. Li, L. et al. Double spiral resonant MEMS scanning for ultra-high-speed miniaturized optical microscopy. *Optica* **10**, 1195–1202 (2023).

17. Zhou, J. et al. An optical fiber-based nanomotion sensor for rapid antibiotic and antifungal susceptibility tests. *Nano Lett.* **24**, 2980–2988 (2024).

18. Li, J. et al. 3D-Printed micro lens-in-lens for in vivo multimodal microendoscopy. *Small* **18**, 2107032 (2022).

19. Guo, X. et al. Full-color holographic display and encryption with fullpolarization degree of freedom. *Adv. Mater.* **34**, 2103192 (2022).

20. Li, J. et al. From lingering to rift: metasurface decoupling for near- and far-field functionalization. *Adv. Mater.* **33**, 2007507 (2021).

21. Liu, Y. et al. Ultracompact metalens-based beam-focusing fiber-optic device with a large numerical aperture. *Opt. Lett.* **48**, 1742–1745 (2023).

22. Liu, Y. et al. Raman spectroscopy fiber probe based on metalens and multimode fiber for malachite green determination. *IEEE Sens. J.* **23**, 16866–16872 (2023).

23. Pahlevaninezhad, H. et al. Nano-optic endoscope for high-resolution optical coherence tomography in vivo. *Nat. Photonics* **12**, 540–547 (2018).

24. Wang, Y., Wan, Y. & Chen, Z. Intravascular photoacoustic and optical coherence tomography imaging dual-mode system for detecting spontaneous coronary artery dissection: a feasibility study. *J. Innov. Opt. Health Sci.* **17**, 2350016 (2024).

25. Gao, L. et al. Endoscopic optical coherence tomography angiography using an externally driving catheter. *J. Biophotonics* **16**, e202300014 (2023).

26. Karnowski, K. et al. Superior imaging performance of all-fiber, two-focusing-element microendoscopes. *IEEE Photonics J.* **14**, 1–10 (2022).

27. Kim, J. et al. Flexible endoscopic micro-optical coherence tomography for three-dimensional imaging of the arterial microstructure. *Sci. Rep.* **10**, 9248 (2020).

28. Wit, J. D., Glentis, G. O. & Kalkman, J. Computational 3D resolution enhancement for optical coherence tomography with a narrowband visible light source. *Biomed. Opt. Express* **14**, 3532–3554 (2023).

29. Wang, W., Ma, J. & Guan, B. Truncated conical-tip fiber probe for commonpath optical coherence tomography with optimal sensitivity. *J. Light. Technol.* **40**, 3974–3979 (2022).

30. Hayama, K. et al. High-depth-resolution imaging of dispersive samples using quantum optical coherence tomography. *Opt. Lett.* **47**, 4949–4952 (2022).

31. Zhao, J. et al. Flexible method for generating needle-shaped beams and its application in optical coherence tomography. *Optica* **9**, 859–867 (2022).

32. Wachulak, P., Bartnik, A. & Fiedorowicz, H. Optical coherence tomography (OCT) with 2 nm axial resolution using a compact laser plasma soft X-ray source. *Sci. Rep.* **8**, 8494 (2018).

33. Yuan, W. et al. Super-achromatic monolithic microprobe for ultrahighresolution endoscopic optical coherence tomography at 800 nm. *Nat. Commun.* **8**, 1531 (2017).

34. Lee, K-S. & Rolland, J. P. Bessel beam spectral-domain high-resolution optical coherence tomography with micro-optic axicon providing extended focusing range. *Opt. Lett.* **33**, 1696–1698 (2008).

35. Wang, W. et al. Miniature all-fiber axicon probe with extended Bessel focus for optical coherence tomography. *Opt. Express* **27**, 358–366 (2019).

36. Li, J. et al. Ultrathin monolithic 3D printed optical coherence tomography endoscopy for preclinical and clinical use. *Light Sci. Appl.* **9**, 124 (2020).

37. Ruchka, P. et al. 3D-printed micro-axicon enables extended depth-of-focus intravascular optical coherence tomography in vivo. *Adv. Photonics* **7**, 026003–026003 (2025).

38. He F. et al. Diffractive metasurface light-shaping from fiber endoscope probes for increased depth of field. In *Proceedings of the Endoscopic Microscopy* XVIII, F, (2023).

39. Vairagi, K. et al. Common-path optical coherence tomography using the Bessel beam from negative axicon optical fiber tip. *IEEE J. Sel. Top. Quantum Electron.* **25**, 1–6 (2018).

40. Vairagi, K. et al. Reflective axicon based energy-efficient extended depth of focus quasi-Bessel beam probe for common-path optical coherence tomography. *Appl. Opt.* **62**, 511–517 (2023).

41. Kim, J. H., Han, J. H. & Jeong, J. C. Common-path optical coherence tomography using a conical-frustum-tip fiber probe. *IEEE J. Sel. Top. Quantum Electron.* **20**, 8–14 (2013).

42. Thampi, A. et al. Towards real time assessment of intramuscular fat content in meat using optical fiber-based optical coherence tomography. *Meat Sci.* **181**, 108411 (2021).

43. Schmitt, J., Knüttel, A. & Bonner, R. Measurement of optical properties of biological tissues by low-coherence reflectometry. *Appl. Opt.* **32**, 6032–6042 (1993).

44. Lu, Y. K. et al. Asymmetric elliptic-cone-shaped microlens for efficient coupling to high-power laser diodes. *Opt. Express* **15**, 1434–1442 (2007).

45. Ding, Z. et al. High-resolution optical coherence tomography over a large depth range with an axicon lens. *Opt. Lett.* **27**, 243–245 (2002).